Chemical Science

ROYAL SOCIETY OF CHEMISTRY

EDGE ARTICLE

View Article Online
View Journal | View Issue

Cite this: *Chem. Sci.*, 2025, **16**, 10990

All publication charges for this article have been paid for by the Royal Society of Chemistry

Received 14th December 2024
Accepted 11th May 2025

DOI: 10.1039/d4sc08461f

rsc.li/chemical-science

Electrosynthesis of molecular memory elements†

Pradeep Sachan,‡[a] Anwesha Mahapatra,‡[a] Lalith Adithya Sai Channapragada,[b] Rajwinder Kaur,[a] Shubham Sahay[b] and Prakash Chandra Mondal *[a]

The increasing pace of computing beyond Moore's law scaling and the von Neumann bottleneck necessitates a universal memory solution that offers high speed, low-power consumption, scalability, and non-volatility, such as resistive switching memristors. However, inconsistencies in the homogeneity and uniformity of surface coverage for switching materials on various electrode substrates, especially those prepared *via* non-covalent methods, result in reduced interfacial stability, thus yielding poor device reproducibility. Electrosynthesis, a reliable and versatile technique for creating covalently bound molecular films on electrode surfaces, enables controlled deposition of large-area, high-quality molecular thin films with nanoscale thicknesses, making it an ideal platform for scalable nanoelectronics. This study explores the electrochemical grafting of two distinct ruthenium complexes: structurally symmetrical [Ru(tpy-ph-NH_2)$_2$](2PF_6)] (**1**) and asymmetrical [Ru(tpy-ph-NH_2)(naptpy)](2PF_6)] (**2**), for the fabrication of large-area, two-terminal molecular junctions intended for resistive switching memory applications. A comparative analysis reveals that **2** exhibits relatively superior memory performance to 1, attributed to its donor–acceptor configuration playing a crucial role. Stable vertical molecular junctions with the configuration ITO/Ru complex$_{24nm}$/Al were fabricated, and electrical measurements were carried out to understand the enhanced switching characteristics. The redox-active molecular devices demonstrate non-volatile resistive switching behavior within a ±3.0 V operation window, featuring a large I_{ON}/I_{OFF} ratio (~10^3), a high power consumption ratio (SET/RESET = 25.5 mJ/75000 mJ), and switching time (SET/RESET = 56/24 ms). Synapse-like potentiation and convolutional neural network simulation were performed, highlighting the potential of these devices for in-memory data processing applications.

Introduction

The Physics and Chemistry Nobel Prizes of 2024 evidenced that Artificial Intelligence (AI) has become an essential component of modern civilization, impacting markets, technology, healthcare, education, and scientific research, reshaping the human–computer interaction strategy.[1] Mead's idea of brain-inspired in-memory computing[2] sparked the search for a new class of devices that could meet the growing demands of technology while overcoming the constraints of the von Neumann bottleneck and Dennard scaling.[3] Resistive random-access memories (RRAM) have emerged as a promising candidate[4,5] in this context, owing to their non-volatile nature[6] with excellent scalability and CMOS compatibility,[7] real-time speed, low operating voltage, long data retention, and simple structure.[8,9] Often termed "memristors" – a concept introduced by Leon Chua in 1971,[10,11] – RRAM refers to nanoscale systems in which electronic and ionic transport are interlinked under the influence of an applied bias, resulting in hysteretic current–voltage (*I–V*) behaviors.[12] It operates through resistive switching, allowing the modulation of device resistance across multiple states in response to an external bias. The compact two-terminal architecture and dense 4F^2 array of this technology address scalability constraints,[13] enhancing processing speed and energy efficiency by co-locating memory and processing functions.[14] A wide range of material choices including organic,[13,15–17] inorganic,[18] clay materials,[19] biomaterials,[20] and metal complexes[21] are well explored as switching materials for RRAM applications. With their customizable molecular designs and low power requirements, organic molecules are emerging as superior next-generation storage technologies. They not only support multi-level storage and synaptic functions (brain-inspired computing) but also offer advantages over inorganic systems in terms of versatility and efficiency. This underscores the critical role of high-quality film fabrication in ensuring stability and extending device lifespan.[22] Molecular memory systems, with tuneable electronic properties, low production costs, mechanical flexibility, high I_{ON}/I_{OFF} ratios, and fast response times, outperform

[a]*Department of Chemistry, Indian Institute of Technology Kanpur, Uttar Pradesh-208016, India. E-mail: pcmondal@iitk.ac.in*

[b]*Department of Electrical Engineering, Indian Institute of Technology Kanpur, Uttar Pradesh-208016, India*

† Electronic supplementary information (ESI) available. See DOI: https://doi.org/10.1039/d4sc08461f

‡ These two authors contributed equally to this work.

other organic systems.[23–26] Redox-active metal-based molecules possess enriching electrochemical and photophysical properties due to metal ion–ligand interaction, allowing adaptable and effective memory behavior with bi- or multistate functionalities.[21,27,28] Memory devices based on redox-active ruthenium (Ru) metal complexes have drawn special attention recently due to their bi-stability, redox state with a high ON–OFF current ratio, high re-writability, solution processability, and chemically tunable functionalities.[29–31] Yet, researchers continue to face challenges in establishing stable and reliable covalent bonds between electrodes and molecules,[32–34] which is crucial for achieving high-performance memory applications. The traditional solution processing techniques like drop casting, spray coating, chemical and physical vapor deposition, ink-jet printing, and spin coating offer large-area deposition but are prone to defects or non-uniformities in the active layer.[35–38] Donor–acceptor metal complexes show potential for high-density memory applications owing to their tunable electronic properties and stable redox behavior. To realize their large-scale integration, scalable architectures like crossbar arrays can be employed, combined with precise electrode patterning and uniform thin film deposition techniques such as electrochemical grafting. These approaches are key to achieving reliable performance and minimizing device variability and crosstalk in memory arrays.

In this work, stable thin films of two different metal complexes, [Ru(tpy-ph-NH_2)$_2$]($2PF_6$) (**1**) and [Ru(tpy-ph-NH_2)(-naptpy)]($2PF_6$) (**2**), that contained donor–acceptor (D–A) moieties were made *via* an electrochemical (E-Chem) deposition method, involving *in situ* diazonium salt preparation. The *in situ* prepared diazonium salts of Ru(II)-polypyridyl-amine complexes were electrochemically converted into aryl radicals that were formed near ITO working electrode surfaces and covalently attached to the working electrode surface, forming oligomeric films. The molecular film thickness can be controlled by varying the electrochemical potential window and scan rates along with the concentration of the aryl diazonium salts.[39,40] Such an E-Chem grafting method has been gaining popularity for creating molecular films of different thicknesses and compositions for studying molecular electronics.[41–43] Besides the thin films of organic molecules, this technique is also suitable for the growth of metal complex films.[44,45] Metal complexes reported in the literature have mostly been grafted on carbon electrodes, including conducting graphite rods, pyrolyzed photoresist films (PPFs), and carbon nanotubes.[46–48] However, ITO is considered an emerging platform for nanotechnological advancements considering its optical transparency (~80% in the visible region), work function closer to metals, and good electrical conductivity that makes it an appropriate substrate for optoelectronic studies.[49] Yet, there are still few reports on E-Chem grafting of redox-active coordination compound-based molecular oligomeric films for advanced nanoelectronics applications. In the present work, we focus on fabricating vertical molecular junctions ITO/Ru(II)-polypyridyl complex/Al for charge transport and memory functions, where molecular layers with varied thicknesses were deposited on ITO, thanks to the electrochemical method, which makes this possible. Thermally deposited Al was chosen as the top electrode due to its high conductivity, good adhesion, low cost, and compatibility with thermal evaporation. Its low work function supports efficient electron injection, resulting in reliable switching characteristics. The D–A-based asymmetric device (ITO/**2**/Al) was studied in-depth for non-volatile memory performance and compared with the molecular junction (MJ) of symmetric ITO/**1**/Al to show the advantages of the D–A-based redox-active metal complex in memory device applications. The [Ru(tpy-phNH_2)(-naptpy)](PF_6)$_2$ metal complex offers superior charge transfer efficiency and enhanced stability compared to conventional organic resistive switching materials. Its intrinsic donor–acceptor (D–A) configuration enables reliable resistive switching, while covalent anchoring ensures the formation of robust thin films. Additionally, it exhibits negative differential resistance (NDR) for neuromorphic applications and has higher thermal and oxidative stability, making it a potential component for futuristic molecular memory devices. This study explores the potential of redox-active D–A ruthenium complexes for non-volatile memory, highlighting their effectiveness, stability, and dependability in next-generation memory devices.

Results and discussion

To explore the potential of redox-active metal complexes with the advantage of multiple redox states for information storage and memory devices, we have designed and synthesized symmetric **1** and asymmetric **2** complexes (Scheme S1†). The structural details of both the complexes were characterized *via* NMR (500 MHz, DMSO-d_6) (Fig. S1–S6†). In the ^{1}H NMR (500 MHz, DMSO-d_6) spectrum of complex **1**, the signals appeared at d (ppm) δ 9.26 (s, 4H), 9.02 (d, J = 8.1 Hz, 4H), 8.18 (d, J = 8.6 Hz, 4H), 8.09–7.91 (m, 4H), 7.47 (d, J = 4.8 Hz, 4H), 7.21 (s, 4H), 6.83 (d, J = 8.6 Hz, 4H), and 5.83 (s, 4H). In the ^{13}C{^{1}H} NMR (500 MHz, DMSO-d_6) spectrum of complex **1**, the signals appeared at d (ppm) 114.62, 119.43, 124.98, 128.06, 129.24, 138.32, 138.51, 152.67, 152.78, 155.31, 158.9, and 162.86. In the ^{1}H NMR (400 MHz, DMSO-d_6) spectrum of complex **2**, the signals appeared at d (ppm) δ 9.61 (s, 1H), 9.54–9.43 (m, 1H), 9.38–9.33 (m, 2H), 9.17–9.07 (m, 4H), 8.73 (s, 1H), 8.64 (s, 1H), 8.56–8.38 (m, 2H), 8.26 (d, J = 8.6 Hz, 2H), 8.13–8.04 (m, 4H), 7.96–7.86 (m, 1H), 7.56 (dt, J = 11.1, 5.6 Hz, 4H), 7.28 (dd, J = 10.3, 4.6 Hz, 4H), 7.19 (dd, J = 15.5, 7.4 Hz, 4H), 6.91 (d, J = 8.5 Hz, 2H), and 5.92 (s, 2H). In the ^{13}C{^{1}H} NMR (500 MHz, DMSO-d_6) spectrum of complex **2**, the signals appeared at d (ppm) 111.89, 114.61, 119.36, 122.86, 125.03, 125.84, 128.06, 128.73, 129.23, 129.42, 130.66, 138.34, 138.48, 147.95, 151.89, 152.51, 155.05, 155.23, 155.65, 158.62, 158.87, 175.22, and 207.33. Further, both complexes were characterized by mass spectroscopy; the mass spectra of complex **1** showed an isotopic pattern with the intensity ratio range from 889.14 to 899.14 (0.13 : 0.059 : 0.062 : 0.34 : 0.45 : 0.59 : 1 : 0.42 : 0.54 : 0.23 : 0.05), and the mass spectra of complex **2** showed an isotopic pattern with the intensity ratio range from 1055.14 to 1069.20 (0.13 : 0.11 : 0.17 : 0.12 : 0.07 : 0.32 : 0.46 : 0.59 : 1 : 0.42 : 0.53 : 0.24 : 0.10 : 0.064 : 0.074), confirming the structure and formation of the desired complexes **1** and **2**, respectively (Fig. S7†). Further

characterization of the metal complexes using thermogravimetric analysis (TGA) reveals good thermal stability of **1** and **2** (Fig. S8†). The sample-to-sample difference in TGA curves for three different batches is shown in Fig. S8c.† The FT-IR spectrum of **1** shows an N–H stretching peak at 3226 cm^{-1} and a C=C stretching peak at 1598 cm^{-1}, while **2** shows two characteristic stretching peaks of C=O and N–H at 1731 cm^{-1} and 3230 cm^{-1}, respectively, corresponding to the amine and carbonyl groups of terpyridine and naptpy ligands, respectively (Fig. S9†). The UV-vis absorption spectra of **1** reveal three peaks centered at 284.95, 378.52, and 502.46 nm, corresponding to π–π*, n–π*, and metal-to-ligand charge transfer (MLCT), respectively. Similarly, **2** reveals three peaks at 285.9, 308.3, and 499.1 nm, corresponding to π–π*, n–π*, and the MLCT band, respectively (Fig. S10†). Additionally, the redox properties of **1** and **2** were investigated by recording cyclic voltammograms using 1 mM of the corresponding complex and 100 mM of $TBAPF_6$ as a supporting electrolyte in anhydrous acetonitrile, employing ITO as the working electrode, a Pt wire as the counter electrode, and $Ag/AgNO_3$ as the reference electrode. **1** displays an irreversible anodic signal at +0.73 V corresponding to the oxidation of the $–NH_2$ group followed by a reversible anodic peak at +1.03 V ($E^{ox}_{1/2}$ = + 0.99 V) *vs.* $Ag/AgNO_3$ corresponding to the $Ru^{2+/3+}$ redox peak. Besides, it shows two ligand-based reductions occurring at −1.32 V and −1.63 V *vs.* $Ag/AgNO_3$ (Fig. S11a†). The redox features of **2** display one irreversible peak at +0.69 V corresponding to the oxidation of the $–NH_2$ group and reversible peaks at + 0.97 V ($E^{ox}_{1/2}$ = + 0.96 V) *vs.* $Ag/AgNO_3$ corresponding to $Ru^{2+/3+}$. It reveals ligand-based reductions appear at −0.83/−0.19 V, the second signal at −1.11/−1.08 V, and the third signal at −1.4/−1.38 V *vs.* $Ag/AgNO_3$ (Fig. S11b†). Custom-patterned ITO electrodes (20 mm × 15 mm) were fabricated on freshly cleaned glass substrates using shadow masks and pulsed DC magnetron sputtering and were subsequently used for electrochemical (E-Chem) grafting (Fig. S12†). By altering the electrochemical potential window and the number of CV cycles, the thickness of the oligomeric films was varied (Fig. S13 and Table S1†). A schematic representation of the thin film preparation of compound **2** *via* aryl diazonium reduction, occurring at −0.46 V *vs.* $Ag/AgNO_3$, along with the electrochemical grafting process, is shown in Fig. 1a and b. The schematics illustrate the preparation and characterization of a thin film on an ITO electrode surface *via* electrochemical grafting with diazonium chemistry. In step (a), the corresponding aryl diazonium salts were reduced at the electrode surface, generating aryl radicals by transferring electrons from the Fermi level (E_F) of the ITO electrode to the diazonium salts. This reduction potential facilitates the formation of highly

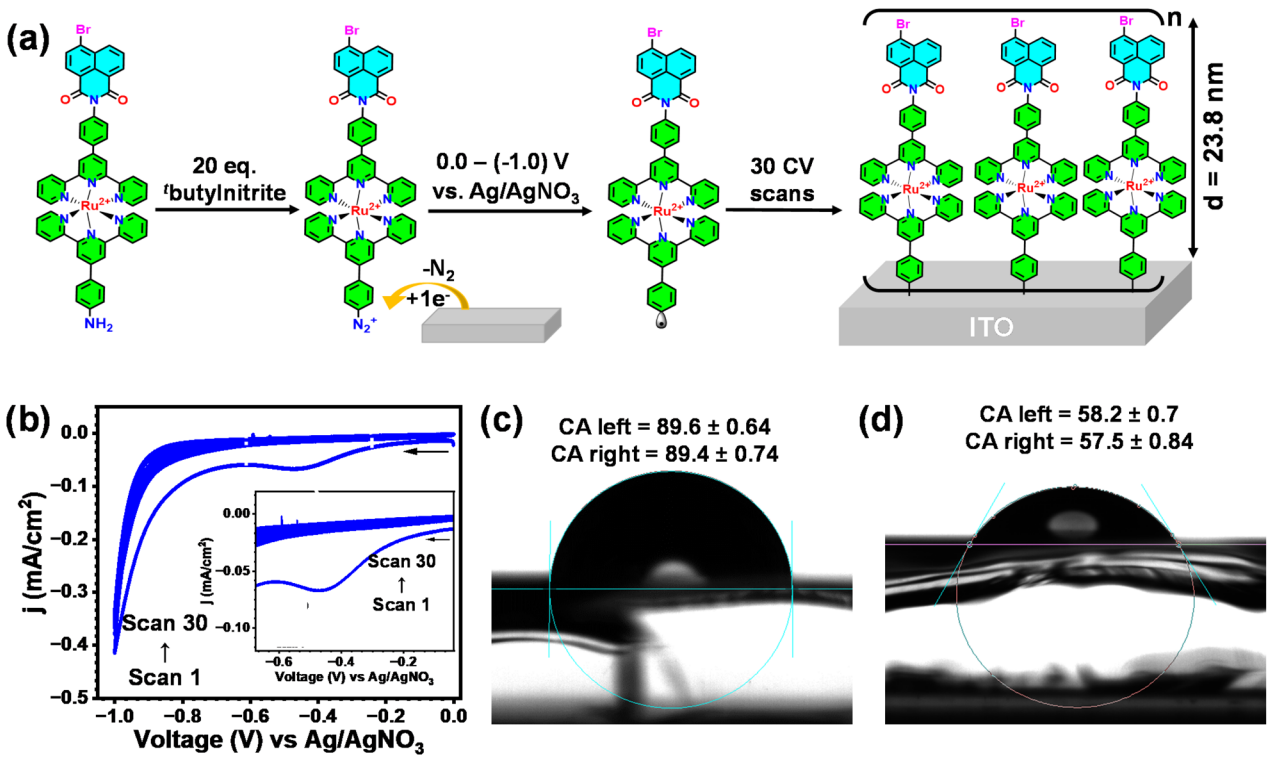

Fig. 1 The preparation and characterization of a thin film on an ITO electrode surface grown *via* an electrochemical grafting method. (a) Corresponding aryl diazonium salts were electrochemically reduced at the ITO working electrode surface, generating aryl radicals. Such reactive radicals form covalent bonds between molecules and ITO electrode surfaces, (b) an electrochemical grafting process was monitored by recording cyclic voltammograms (CVs) up to 30 scans in the potential range of 0 to −1 V (*vs.* $Ag/AgNO_3$), (c) contact angle measurement was performed, by adding a drop of water (2 μL) on blank ITO, and (d) ITO/**2**, to evaluate the surface wettability changes on an ITO electrode surface before and after growing molecular films. On the blank ITO surface, an average contact angle of 89.5° was recorded, indicating a moderately hydrophilic surface. After the ITO underwent electrochemical grafting, the contact angle decreased significantly to an average of 57.85°, showing an increase in hydrophilicity due to the introduction of grafted molecules.

reactive aryl radicals that covalently bind the ITO-electrode surface, creating a stable molecule–ITO interface. This process is advantageous for creating uniform, covalently bonded films, enhancing the stability and conductivity of molecular junctions.[50,51] The electrochemical reduction of Ru(II)-polypyridyl diazonium salts was monitored *via* cyclic voltammetry (CV) for 1–30 scans in the potential range from 0 to −1 V (Fig. 1b). Monitoring multiple CV scans allows for the assessment of grafting efficiency and film growth on the surface of the ITO working electrode. Fig. S14† presents a schematic illustration of the film growth process for complexes **1** and **2** on the ITO surface. The scheme depicts how the aryl diazonium moiety reacts with other sites of the molecule, facilitating film growth up to 27.36 nm for complex **1** and 23.8 nm for complex **2**.[52,53] Both ITO/**1** and ITO/**2** thin films were characterized by UV-vis absorption spectroscopy and compared with solution phase UV-vis spectroscopy. The molecular film thickness-dependent UV-vis absorption spectra of ITO/**1** and ITO/**2** films show two absorption peaks each at λ_{max} = 338.87, 501.32 nm and 339.2, 499.6 nm ascribed to n–π* and MLCT transitions, respectively. Both ITO/**1** and ITO/**2** molecular thin films reveal an increase in the absorbance value as film thickness increases (Fig. S15†). The DFT-optimized molecular structures of **1** and **2** were analyzed using Mercury software (version 4.1.3), indicating a single molecular layer thickness of 18.24 Å for **1** and 24.67 Å for **2** (Fig. S16†). The absorbance increased for ITO/**1** (d = 5.88–27.36 nm) by 187% (thickness from the thinnest to the thickest molecular films) and 243% considering absorbance at λ_{max} = 338 nm and 502 nm, respectively. Based on the experimentally derived film thickness, the number of perpendicular layers can be estimated to be 3 and 15 for the thinnest and thickest oligomeric films (Fig. S17a†). Similarly, the ITO/**2** thin film showed absorbance increases (d = 6.02–23.8 nm) of 134% and 154% at λ_{max} = 334 nm and 499 nm, respectively, with an increased number of perpendicular molecular layers from 3 to 10 (Fig. S17b†). The electrochemical properties of thin films of ITO/**1** and ITO/**2** were further characterized by recording CVs in acetonitrile using 0.1 M $TBAPF_6$ as supporting electrolyte in a potential window of 0–(+1.5) V at a scan rate of 50 mV s^{-1}. Molecularly grafted ITO, Pt wire, and $Ag/AgNO_3$ were used as the working, counter, and reference electrodes, respectively. The CVs of both thin films reveal one reversible redox peak with $E_{1/2}$ values of 1.01 V and 0.98 V (*vs.* $Ag/AgNO_3$) ascribed to $Ru^{2+/3+}$ for **1** and **2** molecular films, respectively (Fig. S18a and b†). The $E_{1/2}$ values are comparable with the electrochemical data of solution phases. The electrochemical stability of both complexes **1** and **2** was carefully examined through CV, which shows no significant degradation or peak shift over five cycles, indicating good electrochemical stability within the operational voltage range (Fig. S18c and d†). The stability of the thin films **1** and **2** on the ITO electrode was tested by subjecting the films to heating up to 180 °C, sunlight exposure for 2 hours, sonication in 5-minute intervals for a total of 60 minutes, and extended testing over a period ranging from 5 days to 1 month (Fig. S19–S22†). In addition, the stability of the thin films **1** and **2** on the ITO electrode was further tested with the help of cyclic voltammetry by sonicating the thin film in an interval of 10 min and exposure to sunlight for 2 h (Fig. S23†). The extraordinary stability of molecular films unequivocally reveals that the films are covalently formed, and such molecular layers are suitable for practical applications. The surface morphology of the molecular film and molecular layer thickness were studied by Atomic Force Microscopy (AFM) by taking line profiles at three different positions of the samples and subtracting the thickness of the bare ITO electrode from the sample thickness. The average molecular film thickness was estimated and tabulated (Fig. S24, S25 and Table S1†).

The Field Emission Scanning Electron Microscopy (FE-SEM) topography image showcases uniform thin films of **2** deposited on ITO substrates (Fig. S26a†). The scale bar indicates a measurement of 500 nm, allowing for size comparison. The surface appears smooth, suggesting a high-quality film growth on the ITO surface with no significant defects or cracks. The cross-sectional FE-SEM image shown in Fig. S26b† was used to measure the thickness of the thin film at three different positions (T1, T2, and T3), which revealed an average thickness for the thickest oligomeric films (Table S2†). Raman spectra were recorded for blank ITO, ITO/1, and ITO/2 thin films and are shown in Fig. S27 and 28.† Fig. 1c, d and S29† show the contact angle measurements where a 2 μL water droplet was placed on a bare indium tin oxide (ITO) surface and an ITO modified surface. The images illustrate the droplet profiles and was used to measure the left contact angles (89.6 ± 0.64 and 58.2 ± 0.7, respectively) and right contact angles (89.4 ± 0.74 and 57.5 ± 0.84, respectively) for each substrate. The average contact angle values were calculated by placing the droplet in various locations across the ITO electrode to ensure consistent wettability assessment. The comparison highlights changes in surface hydrophilicity due to the modifications of **2**. The increase in hydrophilicity due to the introduction of grafted molecules suggests that the surface energy of the ITO electrode was altered by the grafting process, which likely introduced polar functional groups, and the presence of counter anions ($2PF_6$ per Ru^{2+} ion), enhancing the electrode's affinity for water. This shift in the contact angle can be an important indicator of successful film formation.

Theoretical studies

Gaining insight into the detailed electron energy level structure of a molecular system is essential for understanding its electrical properties. The lowest energy level available for electron occupation and the highest energy level inhabited by electrons in molecular systems are denoted by the LUMO (Lowest Unoccupied Molecular Orbital) and HOMO (Highest Occupied Molecular Orbital), respectively. The HOMO, which contains the most loosely bound electrons, frequently promotes charge transfer and chemical processes, whereas the LUMO accepts on electrons. The band gap and HOMO/LUMO energy levels of **1** and **2** were experimentally determined by combining UV-vis spectroscopy on oligomeric films deposited on ITO and cyclic voltammetry (CV) measurements with respect to ferrocene (Fig. S30 and S31†). The optical band gap for the thickest oligomeric films was estimated to be 2.29 eV for **1** (d = 27.36 nm)

and 2.21 eV for **2** (d = 23.8 nm). Based on the ferrocene redox peak and the first onset reduction potential of both the metal complexes, the HOMO and LUMO energy levels were calculated.[42,54] For **1**, the HOMO and LUMO energies are −5.82 eV and −3.53 eV, respectively, and for **2**, they are −5.53 eV and −3.32 eV. To further validate the experimental results, the frontier molecular orbitals of **1** and **2** were optimized using density functional theory (DFT) calculations. **1** was optimized with the B3LYP level 6-31G** basis set for the ligands (C, H, and N) and the SDD basis set for Ru(II) and then studied using Chemcraft software,[55,56] as shown in Fig. S32.† Similarly, **2** was optimized with the help of the B3LYP level 6-31G** basis set for the ligand (C, H, N, O, and Br) and the SDD basis set for Ru(II) metal, and further studied with the help of Chemcraft.[57] As illustrated in Fig. 2, the HOMO electron density in compound **2** is primarily concentrated around the Ru(II) center, whereas the LUMOs are mainly localized on the naptpy group. The energy gap between the HOMO and LUMO of **2** was found to be 3.04 eV, which demonstrates that upon the coordination of the naptpy ligand to the **2** complex cores, a narrowed energy gap led to improved stabilization of the systems. The calculated energies of the frontier orbitals of **1** and **2** are presented in Table S3.† To interpret the experimental UV-vis data, TD-DFT calculations were conducted using the B3LYP functional in combination with the 6-31G and SDD basis sets.[56] The optimized geometries of the ground state were used for TD-DFT calculations,[58] under CH_3CN solvent. The experimental and theoretical UV-vis spectra of **1** and **2** are shown in Fig. S33.† The TD-DFT results showed that **1** and **2** complexes exhibited a major absorbance band at λ_{max} = 336.5 and 349.7 nm with oscillator strengths of 0.1842 and 0.5582 and two low-intensity bands at 443.47 and 430.35 nm with oscillator strengths of 0.2742 and 0.3127, respectively. In summary, TD-DFT results demonstrate that the experimentally observed absorbance bands align well with the calculated electronic transitions. The electronic charge density distribution was visualized by mapping the changes in the electrostatic potential (ESP) over the total electron density.[59] The ESP plots **1** and **2** illustrate electronic potential using colour gradients, where red denotes regions of high electron density and blue signifies areas with low electron density (Fig. S34†). Electron density in **1** is symmetrically distributed across both sides of the terpyridine ligand. In contrast, **2** shows a shift in electron density towards the naptpy ligand, indicating an asymmetric electron distribution.

X-ray photoelectron spectra

The X-ray photoelectron spectra (XPS) analysis confirmed the chemical composition of the molecular thin film on the ITO electrode. The full survey scans of both ITO/**1** and ITO/**2** thin films are displayed in Fig. S35.† The survey scan of ITO/**1** shows the presence of various elements, including Ru 3d, C 1s, N 1s, P 2p, and F 1s. The XPS spectra of C 1s, N 1s, and Ru 3d were deconvoluted and fitted, as shown in Fig. S36.† The C 1s spectrum was deconvoluted into two peaks: a higher-intensity peak at 284.60 eV, corresponding to C–C/C=C, and a peak at 285.33 eV, attributed to carbon bonded to an electronegative atom (C=N). The Ru 3d peaks are masked under the C 1s spectrum, displaying two peaks at 280.67 eV and 284.87 eV, corresponding to Ru(II) $3d_{5/2}$ and Ru(II) $3d_{3/2}$ states, with a spin–orbit coupling of 4.2 eV (Fig. S36a†). The XPS spectrum of ITO/**2** shows the presence of Ru 3d, C 1s, N 1s, O 1s, Br 3d, P 2p, and F 1s elements in the film.[42,54] The C 1s spectra were deconvoluted into four peaks at 284.76, 285.65, 286.47, and 287.55 eV attributed to different carbon bonds. The peak with strong intensity appearing at binding energy = 284.78 eV corresponds to the C–C/C=C peak, while the peaks at 285.65, 286.47, and 287.55 eV,

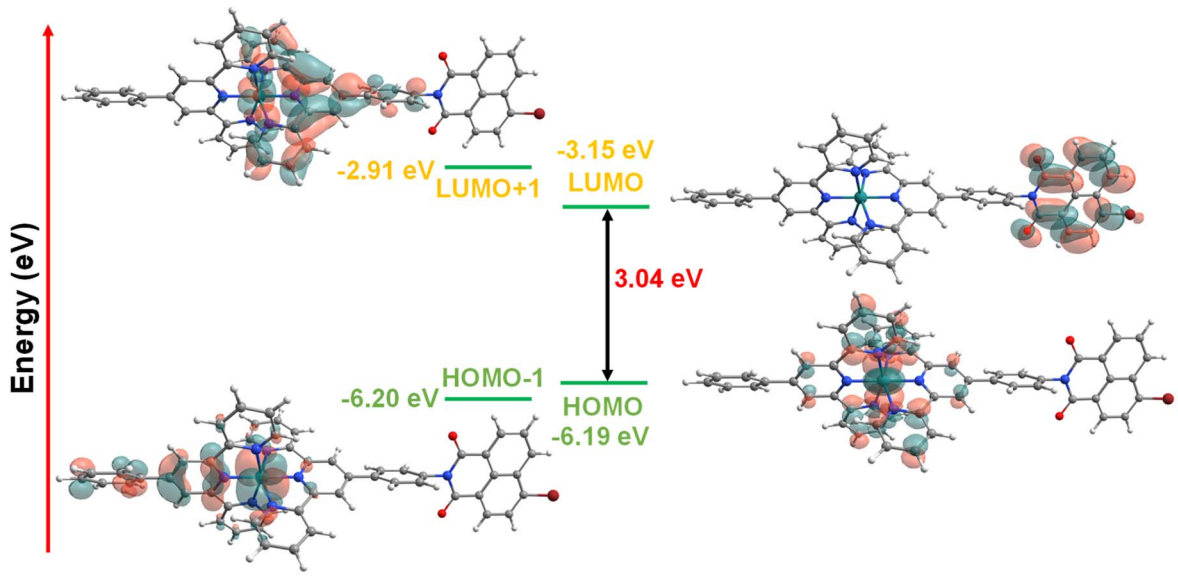

Fig. 2 The energy level diagrams of the $[Ru(tpy\text{-}ph)(naptpy)]^{2+}$ complex calculated at the B3LYP functional level using the 6-31G** and SDD basis sets for the ruthenium complex; the data were analyzed by using Chemcraft software. The positions of the HOMO, the LUMO, and their energy gap are shown in eV.

i.e., higher binding energies, correspond to a carbon atom attached to an electronegative atom like nitrogen, bromine, and oxygen, respectively. The peaks of Ru 3d are masked under the C 1s spectrum, which displays two distinct peaks at 281.03 eV and 285.14 eV. These peaks correspond to the Ru(II) $3d_{5/2}$ and Ru(II) $3d_{3/2}$ states, with a spin–orbit coupling of 4.11 eV, as shown in Fig. 37a.† Nitrogen peaks at 400.06 and 399.51 eV reveal coordinated nitrogen (N_c) and N–C=O groups of the ligand (Fig. 37b†). The XPS spectrum of O 1s reveals one peak at 532.02 eV for the presence of the C=O bond (Fig. 37c†). In addition, the peak at 71.87 eV corresponds to the bromine atom bonded with the carbon confirming the presence of one Br in the naphthalene ring (Fig. 37d†). The thin film of complex **2** exhibits an estimated elemental ratio of Ru : N : Br (1 : 3.38 : 1.06). In XPS analysis, the observed Ru : N : Br ratio deviates from the expected stoichiometry, which might arise due to differences in absorption cross-sections and surface sensitivity of the elements. Ru and Br produce stronger signals due to their higher cross-sections and surface accessibility. Nitrogen, being lighter and possibly buried beneath heavier atoms, shows weaker intensity.[60,61]

Memory device analysis

This study successfully demonstrated bipolar resistive switching in ITO/**2**/Al molecular junctions with an active area of 0.25 mm^2 (Fig. S38–40† and 3a). Devices that consist of a 23.8 nm molecular layer were characterized for current density–voltage behavior using a potential sweep in a ±3.0 V range, with a 1.2 V s^{-1} scan rate (Fig. S41†). The current density–voltage (*j*–*V*) characteristics of the device display a sharp increase in current at the threshold voltage, signaling a transition from a high resistance state (HRS) to a low resistance state (LRS). In the semi-log plot (Log *j*–*V*) for the voltage sweep from 0 to +3.0 V (Fig. 3b), hysteresis was observed, with an abrupt rise in current at +2.87 V occurring in 56 ms, indicating resistive switching behavior. This transition, corresponding to the SET (Write) process, marks the change in conductance from the OFF (low conductance) to the ON (high conductance) state. While sweeping back from +3.0 to −3.0 V, the high-conductance state corresponding to the "Read" process is retained until it reaches a negative threshold voltage (−1.79 V). The device shows an abrupt fall in current from the LRS to the HRS at −1.79 V in 24 ms, which indicates the RESET (Erase) procedure. An I_{ON}/I_{OFF} ratio ~10^3 is calculated from the hysteresis shown in Fig. 3b. Energy consumption for SET and RESET processes is 25.5 mJ (0.159 mA at +2.87 V) and 75 000 mJ (1760 mA at −1.79 V), respectively, yielding a RESET/SET energy consumption ratio >10^3. The device with a vertical configuration of ITO/**2**/Al contains 20 RRAM MJs in a single chip with a yield of 65% (in terms of working devices, Table S5†). The ITO/**2**/Al MJ-based devices were tested in different sets of batches to ensure the reproducibility, reliability, and stability of the memory performance of the device. It helps assess device variability, optimize fabrication processes, validate statistical consistency, and check environmental effects for real-world applications (Fig. S42 and Table S6†). The uniformity of the switching parameters for the ITO/**2**/Al device was checked at four different junctions

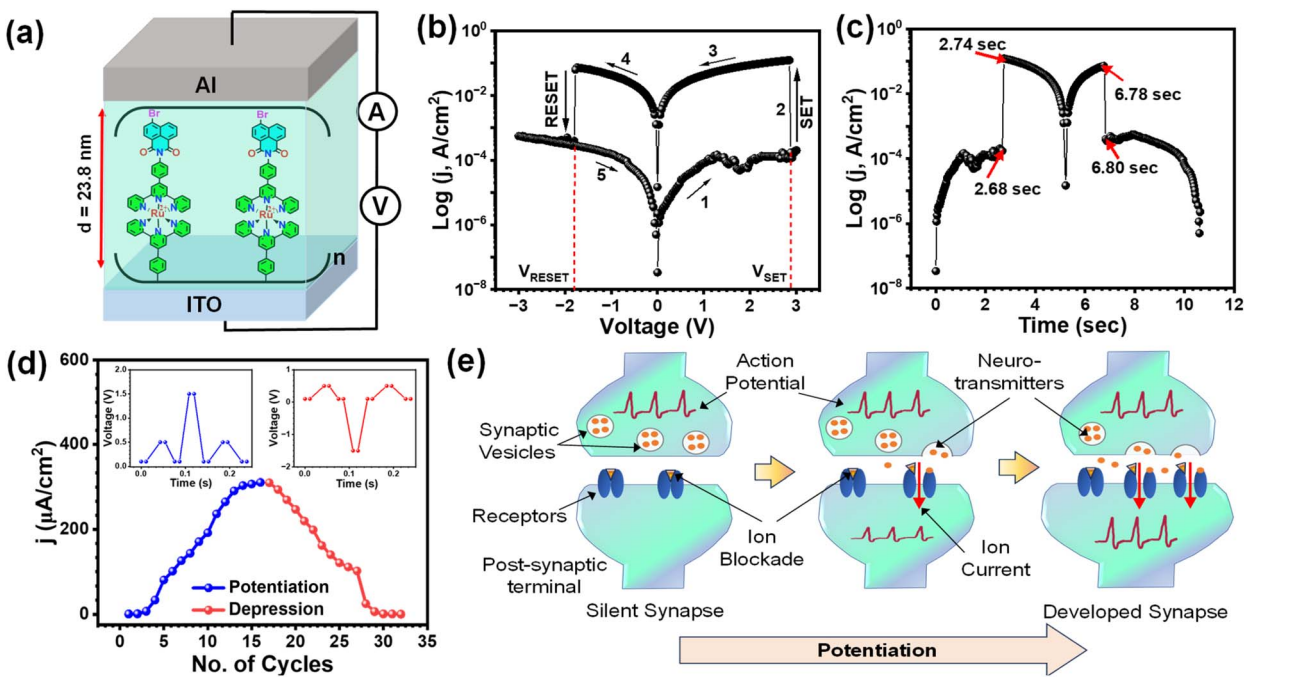

Fig. 3 Resistive switching characteristics of the ITO/**2**/Al molecular device configuration for memory applications. (a) Side view of two-terminal MJs with vertical stacking of ITO/$\mathbf{2}_{d=23.8nm}$/Al with an active area of 0.25 mm^2 for memory characteristics, (b) a typical semi-log plot of current density–voltage of the ITO/**2**/Al MJs showing resistive switching within a ±3.0 V potential window, (c) semi-log plot of current density with respect to time, (d) potentiation and depression measurement of the device using read-only pulses at +0.5 V following write pulses of +1.5 V or erase pulses of −1.5 V, and (e) potentiation in biological synapses as a result of weight enhancement by repetitive excitation.

(Fig. S43†). The statistical distribution of SET and RESET voltages for the ITO/2/Al device was analyzed across three batches, comprising a total of eighteen molecular junctions (Fig. S44†). To check the scan rate-dependent memory behavior of ITO/**2**/Al, the *j*–*V* curves were recorded at different scan rates, which suggested that a higher scan rate typically shifts the SET and RESET potentials towards higher voltage due to charge trapping and capacitive effects. It can also broaden the hysteresis loop, suppress intermediate states, and affect switching dynamics. Lower scan rates allow full relaxation, leading to more stable and efficient switching (Fig. S45†). Our devices (ITO/**2**/Al) show DC endurance for up to 110 cycles with a retention time of 82 s at a read voltage of +0.5 V, with a write pulse of +5.0 V and an erase pulse of −3.5 V (Fig. S46†). The response speed of memory devices can be improved by optimizing key factors such as incorporating electron-rich or -deficient groups to lower charge transport barriers, enhancing the electrode–molecule interface and precisely controlling film thickness and morphology through techniques like electrochemical grafting. Nanoscale device architectures (*e.g.*, crossbar arrays) and tuning input pulse parameters can further accelerate switching. We plan to systematically investigate these strategies in future work to enhance device performance.

The control experiment was performed with ITO/Al junctions without any molecular layers, and it confirmed the role of **2** as a switching material for resistive non-volatile memory applications (Fig. S47†). The device performance has been compared with that of the fabricated ITO/**1**/Al device, where symmetric molecules are used as the switching material (the corresponding device performance is shown in Fig. S48†). As compared to the ITO/**1**/Al device, the D–A redox-active molecule-containing (ITO/**2**/Al) device shows an ∼10 times higher I_{ON}/I_{OFF} ratio. The performance of both symmetric and asymmetric devices was calculated and compared with the existing literature and are shown in Tables S7 and S8.† Fig. 3c shows the semi-log plot of the current density with respect to time and as observed, the device takes 56 ms to SET (HRS to LRS) and 24 ms to RESET (LRS to HRS). Fig. 3d shows an example of the potentiation and depression measurement in the memory switching devices. When alternating Write and Read pulses were applied at +1.5 V and +0.5 V at 100 ms intervals, the results showed a consistent increase in the Read current, indicating DC potentiation effects up to 16 cycles. This was followed by a depression measurement, which shows DC depression up to 16 cycles at Erase and Read pulses of −1.5 V and +0.5 V, respectively. Fig. 3e shows a schematic representation of the potentiation effect in the chemical signaling pathway of a biological synapse.[62,63] Potentiation refers to the strengthening of synaptic transmission between neurons, which enhances the efficiency and magnitude of signaling. The release and capture of neurotransmitters control the chemical signal transmission in the biological synapse. In this process, information is mostly transferred from one cell to its adjacent cell *via* receptors consisting of ion channels. Potentiation of synaptic transmission occurs *via* the following steps. First, with no communication between the two terminals, a synapse is silent.[64] The arrival of an action potential at the pre-synaptic terminal triggers the release of neurotransmitters from the vesicles. These released neurotransmitters bind to the receptors of the postsynaptic terminal, removing the ion blockade and allowing calcium ion (Ca^{2+}) influx.[65] Thus, electrical signals are transmitted from one neuron to the next. The ionic current in the postsynaptic cell triggers a series of neurochemical reactions, leading to events like the growth or removal of receptors. With repeated excitatory signals, the number of receptors at the post-synaptic terminal increases.[66] Additionally, it may enhance vesicle fusion with the presynaptic membrane, releasing more neurotransmitters into the synaptic cleft.[67] Hence, the synapse develops in size and strength, resulting in the corresponding weight enhancement, increasing the magnitude of the signaling between two terminals.[64] The opposite phenomenon decreasing the synaptic strength due to repeated inhabitation is called depression.

To analyze the conduction mechanism responsible for the resistive memory behavior of the ITO/**2**/Al device, the *j*–*V* curves for SET (Fig. 4a) and RESET (Fig. 4b) were plotted separately under positive and negative bias conditions on a logarithmic scale. These plots were subsequently fitted with linear models, providing valuable insights into the relationship between current and voltage behavior within the device.[68] Under positive bias (SET conditions), the device initially exhibited low charge injection at lower voltages. However, as the applied voltage increased, the charge injection also increased, leading to a sharp rise in current. For the thermally produced charge carriers, the current density (*j*) follows the ohmic conduction mechanism[69] as expressed by

$$j = \frac{qn_0\mu V}{d} \quad (1)$$

The space charge limited current[70] (I_{SCLC}) on the other hand can be expressed as

$$I_{SCLC} \sim \chi_S \mu \frac{V^2}{d^3} \quad (2)$$

where q is the charge of the carrier, n_0 is the free carrier density, μ is the carrier mobility, χ_s represents the dielectric constant of the molecular layer, and d stands for molecular layer thickness. The two distinct slopes were observed in the HRS under positive bias; at a lower voltage (<0.12 V), $m = 0.75$ ($I_{SCLC} \sim V$), which follows the ohmic model and follows equation (i). As voltage increases, the slope becomes $m = 1.73$ ($I_{SCLC} \sim V^2$) and current behavior follows equation (ii). The ohmic conduction mechanism predominates at low applied bias because of thermally generated free electrons in the molecular film; in the high-voltage region, on the other hand, the quadratic correspondence between voltage and current (Child's Law) suggests that some electrons passed through the dielectric layers and were trapped, resulting in space-charge-limited current (SCLC). The observed change in resistance is caused by the traps capturing and releasing electrons at a specific energy level.

However, in the LRS, under positive bias, with $m = 1.0$ ($I_{SCLC} \sim V$), an ohmic conduction mechanism is followed as the current shows linear variation with the applied bias, indicating a conducting pathway formation.[71] As shown in Fig. 4a, at low

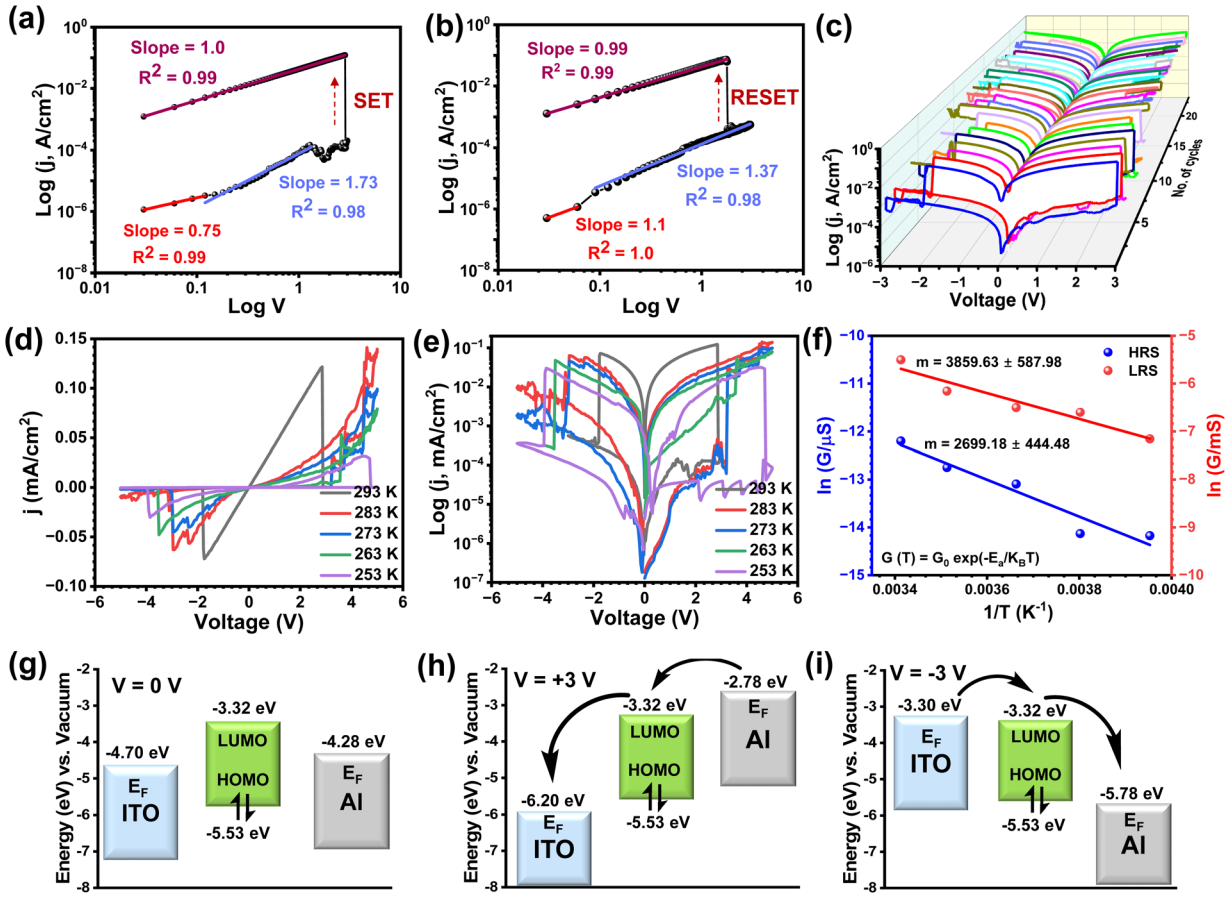

Fig. 4 Charge conduction mechanism of resistive switching memory devices. (a) Experimental and fitted log j *versus* log V plot of ITO/**2**/Al devices under SET conditions and (b) RESET conditions, (c) semi-log plot of the ITO/**2**/Al molecular junction for cycling stability up to 23 cycles, (d) I–V data at various temperatures (293, 283, 273, 263, and 253 K), (e) temperature dependent semi-log plot of current density *vs.* voltage, (f) Arrhenius plot of the HRS and LRS conductance measured in between 293 and 253 K. The activation energies (E_a) for the LRS and HRS are calculated from the slope of the linear fits for ln($G/\mu S$) *vs.* T^{-1} (K), (g) proposed charge transport mechanism in ITO/**2**/Al MJ devices by the Fermi energy level of the electrode and frontier molecular orbitals and the devices under isolated conditions (at 0 V), and (h and i) energy profile of the devices at +3.0 V and −3.0 V. The energy landscapes shown here are with respect to the vacuum level.

voltages, the ITO/**2**/Al device exhibits ohmic behavior with slopes in the LRS (m = 0.99) and HRS (m = 1.1), indicating a linear current–voltage relationship. At higher voltages (V > 1.37 V), the device transitions to a quadratic dependence of current on voltage ($I \sim V^2$), consistent with space-charge-limited conduction behavior. The cycling stability of the ITO/**2**/Al device was evaluated over 23 cycles, demonstrating consistent performance, as shown in Fig. 4c. These data indicate good reliability across repeated switching operations. In addition, the device was tested across a range of temperatures (293, 283, 273, 263, and 253 K) to investigate the underlying switching mechanism. The ITO/**2**/Al memory device exhibited a clear trend: both SET and RESET voltages increased with decreasing temperature, which is characteristic of donor–acceptor-based systems due to reduced thermal activation and slower charge transfer dynamics. A significant decrease in OFF-state current was observed, while the ON-state current remained relatively stable, resulting in an enhanced ON/OFF ratio. This behavior can be attributed to suppressed thermally activated hopping in the OFF state (Fig. 4d and e). Furthermore, temperature-dependent I–V data were utilized to estimate the activation energy (E_a) by plotting the semi-logarithm of conductance *versus* the inverse of temperature.[72] The ITO/**2**/Al memory device shows a slope of m_{LRS} = 3859.63 ± 587.98 and m_{HRS} = 2699.18 ± 444.48. The activation energy, E_a for ON and OFF states are calculated at 333 ± 51 m eV and 233 ± 38 m eV, respectively (E_a = slope × K_B, where $K_B = 8.617 \times 10^{-5}$ eV K^{-1}).[73] These values suggest trap-assisted switching and the presence of negative differential resistance in the device under discussion.[74] Further, the switching mechanism of ITO/**2**/Al MJ was investigated based on the energy profile diagram. The energy profile diagram under isolated conditions shows the Fermi energy (E_F) levels of the ITO (bottom) and Al (top) electrodes, along with the HOMO and LUMO energies of molecule **2** (Fig. 4g–i). When a positive bias ranging from 0 to +3.0 V range is applied, the E_F of the bottom electrode (ITO) shifts downward, and the E_F of the top electrode (Al) shifts upward. At negative bias, the E_F of the Al top electrode reaches 2.78 eV as it becomes populated with electrons, enabling electron transfer from the top electrode to the LUMO and then to the bottom electrode. Conversely, at −3.0 V, the E_F

of the bottom electrode becomes populated with electrons under negative bias, resulting in electron transfer from the bottom electrode to the LUMO and subsequently to the top electrode.

Electrochemical impedance spectra

AC-based electrochemical impedance spectra (EIS) of the MJs were used to analyze the frequency-dependent electrical response of the electronic device.[75,76] According to the principle of EIS, the impedance of a pure resistor is a frequency-independent device, which holds $Z_{imp} = R$, with a phase angle of 0° with respect to the AC amplitude. For an ideal capacitor ($X_C = 1/j\omega CPE$) (where $j = \sqrt{-1}$, and CPE stands for constant phase element), the phase angle is shifted by 90°. EIS reveals the real components of the molecular junction, such as contact resistance (R_C), constant phase element (CPE), and resistive nature of the molecular junction (R_{MJ}). We performed EIS on a 23.8 nm thick ITO/2/Al MJ across a frequency range of 10^5 Hz to 1 Hz with a fixed sinusoidal signal with an amplitude of 100 mV and varying DC voltages (0, 5, 10, 20, 50, and 100 mV) between the two electrodes. Both experimental and fitted data of Nyquist (Z_{real} *vs.* $Z_{imag.}$) and Bode (Z_{real} *vs.* frequency and phase angle *vs.* frequency) plots at different voltages are shown in Fig. 5a–c, respectively. The Nyquist plot gives R_c by plotting the real part on the *x*-axis and the imaginary part on the *y*-axis. The EIS data were fitted with the Randles circuit model using Metrohm electrochemical analyst software, where R_{MJ}, R_C, and CPE components correspond to the molecular layer resistance, contact resistance, and capacitance element of the MJ. The equivalent circuit model comprises an uncompensated resistance ($R_C = 103\ \Omega$) in series with a parallel combination of two constant phase elements (CPEs) and resistors. The model shows a good fit to the experimental data, with a Kramers–Kronig-derived goodness-of-fit value of 4.3×10^{-3} at 0 mV. The EIS measurements were performed under varying DC bias voltages (0, 5, 10, 20, 50, and 100 mV), with the corresponding fitting results presented in Fig. 5a–c and Table S9†. The Bode plot allows us to comprehend both the real impedance and the phase angle as a function of frequency. For example, the data indicate that the junction exhibits resistive behavior at lower

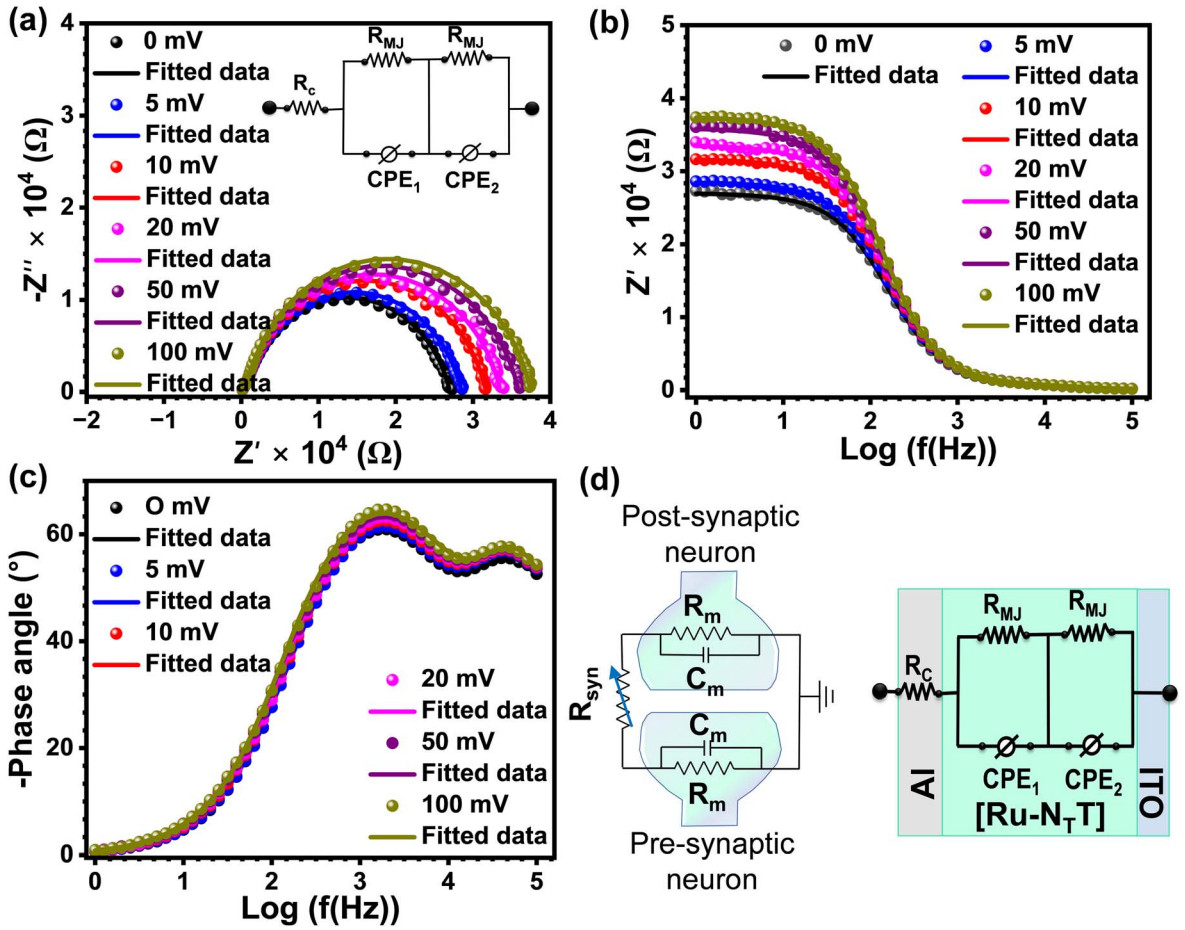

Fig. 5 EIS measurements for the ITO/2/Al MJ in the frequency range from 10^5 Hz to 1 Hz at an AC amplitude of 100 mV and varying DC voltages of 0, 5, 10, 20, 50, and 100 mV applied between the bottom and top electrodes. (a) Nyquist plot with Randles's equivalent circuit model used for data fitting. The EIS data illustrate the frequency-dependent response of the CPE and the resistance of the MJ (inset), (b and c) Bode plot, and (d) electrical model of a synapse (left) in terms of membrane resistance (R_m), membrane capacitance (C_m), and synaptic resistance (R_{syn}) compared with the Randles's equivalent circuit model of the ITO/2/Al MJ (right).

frequencies, while at higher frequencies, it demonstrates a capacitive response.

Fig. 5d (left) shows an equivalent electrical model of a chemical synapse, where R_m is the membrane resistance, C_m is the membrane capacitance, and R_{syn} is the synaptic resistance.[77] Typically, R_m is taken as 3.3 kΩ cm^2 and C_m is as 1 μF cm^{-2} with an average synaptic width of 0.2 μm.[78] R_{syn} changes with the amplitude and frequency of the action potential.[64] With heightened/frequent excitatory input, R_{syn} decreases, increasing the conductance (*i.e.*, weight) of the synapse. As a result, the post-synaptic current increases. For low amplitude and delayed excitation, the R_{syn} increases, decreasing the synaptic weight. The equivalent circuit model of the ITO/**2**/Al MJ is shown on the right for the sake of comparison.

Convolutional neural network simulation

We have utilized the proposed device as a synaptic element representing the weights for *ex situ* training of a Convolutional Neural Network (CNN). A linear mapping was established between the model weights [W_{min}, W_{max}] and the experimentally measured conductances [G_{min}, G_{max}] for the proposed device. The potentiation and depression characteristics of the device shown in Fig. 6, represented as discrete increasing and decreasing conductance states, respectively, were used to define the allowed conductance states of the trainable parameters. Training was performed using categorical cross-entropy loss. In each epoch, the forward pass computed the prediction and loss (L), and backpropagation yielded the gradient with respect to each trainable parameter. Conductance updates were performed according to both the sign and magnitude of the gradient. The trained CNN based on the proposed device implementing synaptic weights was evaluated on the MNIST handwritten digit classification task.[79–81] The MNIST dataset consists of 28 × 28 pixel images of handwritten digits with 60 000 training images and 10 000 test images. The CNN based on the proposed device as the synaptic element achieved a test accuracy of 98.18%, exhibiting minor degradation compared to the ideal floating-point software baseline, which attained an accuracy of 99.01%, as shown in Fig. 6.

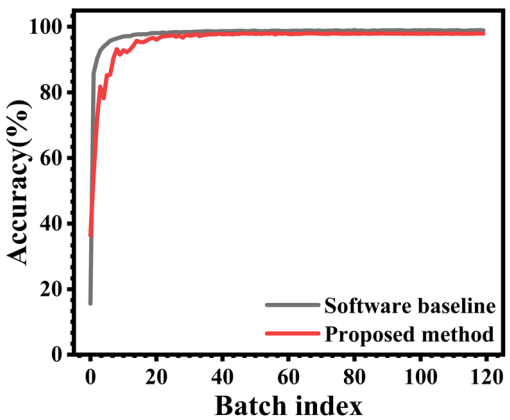

Fig. 6 Test accuracy as a function of batches trained for the proposed synapse-based training method (red) and the floating-point software baseline (gray). The comparable convergence profiles demonstrate the robustness of our method.

Conclusions

Resistive switching offers a promising solution to the von Neumann bottleneck and Moore's law limitations in traditional digital computing. Arranged in a crossbar array, it leverages history-dependent conductance to store data and performs vector-matrix operations, with Kirchhoff's and Ohm's laws enabling summation and multiplication.[1] This architecture supports synapse-like plasticity and in-memory computing,[14] offering a pathway toward more efficient data processing. Transition-metal complexes outperform their oxide counterparts as switching materials in this architecture offering bi- or multi-stable resistive states[21] due to their highly tuneable electrical properties, driven by the interplay between metal ions and ligands. However, achieving uniform and homogeneous switching layers on the nanoscale remains a challenge.[26] Electrosynthesis offers a cost-effective, scalable method for direct synthesis of thin, crack-free films,[82] allowing precise control over reagent activity by adjusting the electrode potential, making it ideal for synthesizing new complexes on a large scale with low cost.[83]

Thus, electrochemical grafting of metal complexes is a promising pathway for developing high-performance, nanoscale memory devices. The fabricated molecular junctions exhibit stable non-volatile resistive switching with a high I_{ON}/I_{OFF} ratio, low power consumption, and good cyclic endurance, all within a compact operational potential window. Harnessing the synaptic behavior of these systems reveals their potential in neuromorphic technology. These concepts underscore the effectiveness of using electrosynthesized metal complexes to overcome key limitations in device yield and stability, advancing the feasibility of commercial device fabrication beyond the scaling limits of conventional technology.

Data availability

The data supporting this article have been included as part of the ESI.†

Author contributions

P. S.: conceptualization, investigation, and writing – original draft. A. M.: writing & investigation. LASC performed the simulation for CNN. R. K.: writing & investigation. S. S. supervised the CNN simulation. P. C. M.: funding, supervising, and writing – review & editing. The manuscript was written through the contributions of all authors. All authors have approved the final version of the manuscript.

Conflicts of interest

There are no conflicts to declare.

Acknowledgements

P. S. thanks the Council of Scientific & Industrial Research (CSIR), New Delhi, for a senior research fellowship (Fellowship No. CSIR/EMR-I/2019/09/092(1033)). A. M. and P. C. M. acknowledge the Government of India for the Scheme for Transformational and Advanced Research in Sciences (STARS) (Grant No. STARS-2/2023-0535) for funding. R. K. thanks the University Grants Commission for a senior research fellowship (NTA Ref. No. 211610012732). The authors thank IIT Kanpur for providing access to its infrastructure and instrumentation facility.

References

1 A. Mehonic, D. Ielmini, K. Roy, O. Mutlu, S. Kvatinsky, T. Serrano-Gotarredona, B. Linares-Barranco, S. Spiga, S. Savelev, A. G. Balanov, N. Chawla, G. Desoli, G. Malavena, C. Monzio Compagnoni, Z. Wang, J. J. Yang, S. G. Sarwat, A. Sebastian, T. Mikolajick, S. Slesazeck, B. Noheda, B. Dieny, T.-H. (Alex) Hou, A. Varri, F. Brückerhoff-Plückelmann, W. Pernice, X. Zhang, S. Pazos, M. Lanza, S. Wiefels, R. Dittmann, W. H. Ng, M. Buckwell, H. R. J. Cox, D. J. Mannion, A. J. Kenyon, Y. Lu, Y. Yang, D. Querlioz, L. Hutin, E. Vianello, S. S. Chowdhury, P. Mannocci, Y. Cai, Z. Sun, G. Pedretti, J. P. Strachan, D. Strukov, M. Le Gallo, S. Ambrogio, I. Valov and R. Waser, *APL Mater.*, 2024, **12**, 109201.

2 C. Mead, *Proc. IEEE*, 1990, **78**, 1629–1636.

3 I. L. Markov, *Nature*, 2014, **512**, 147–154.

4 F. Zahoor, T. Z. Azni Zulkifli and F. A. Khanday, *Nanoscale Res. Lett.*, 2020, **15**, 90.

5 M. Ziegler, *Nat. Electron.*, 2019, **2**, 561–562.

6 M. L. Varshika, F. Corradi and A. Das, *Electronics*, 2022, **11**, 1610.

7 S. Ambrogio, S. Balatti, V. Milo, R. Carboni, Z. Q. Wang, A. Calderoni, N. Ramaswamy and D. Ielmini, *IEEE Trans. Electron Devices*, 2016, **63**, 1508–1515.

8 S. Kumar, X. Wang, J. P. Strachan, Y. Yang and W. D. Lu, *Nat. Rev. Mater.*, 2022, **7**, 575–591.

9 R. Waser, R. Dittmann, S. Menzel and T. Noll, *Faraday Discuss.*, 2019, **213**, 11–27.

10 *Advances in Neuromorphic Memristor Science and Applications*, ed. R. Kozma, R. E. Pino and G. E. Pazienza, Springer Science & Business Media, 2012.

11 L. Chua, *IEEE Trans. Circuit Theory*, 1971, **18**, 507–519.

12 D. B. Strukov, G. S. Snider, D. R. Stewart and R. S. Williams, *Nature*, 2008, **453**, 80–83.

13 K. Y. Cheong, I. A. Tayeb, F. Zhao and J. M. Abdullah, *Nanotechnol. Rev.*, 2021, **10**, 680–709.

14 D. Ielmini and H.-S. P. Wong, *Nat. Electron.*, 2018, **1**, 333–343.

15 Y. Li, Q. Qian, X. Zhu, Y. Li, M. Zhang, J. Li, C. Ma, H. Li, J. Lu and Q. Zhang, *InfoMat*, 2020, **2**, 995–1033.

16 L. Yuan, S. Liu, W. Chen, F. Fan and G. Liu, *Adv. Electron. Mater.*, 2021, **7**, 2100432.

17 M. Akshaya, D. Harshini, R. Gayathri, P. M. Imran and S. Nagarajan, *ACS Appl. Electron. Mater.*, 2024, **6**, 7522–7539.

18 *Resistive Switching: Oxide Materials, Mechanisms, Devices and Operations*, ed. I. V. Jennifer Rupp, D. Ielmini, Springer US, 2022.

19 F. Y. Rahman, S. Chakraborty, R. Deb, M. J. Uddin, D. Bhattacharjee, K. A. Alibrahim, A. N. Alodhayb and S. A. Hussain, *ACS Appl. Electron. Mater.*, 2024, **6**, 6591–6607.

20 F. Y. Rahman, R. Deb, S. Sarkar, H. Banik, M. J. Uddin, S. Chakraborty, D. Bhattacharjee and S. A. Hussain, *ACS Appl. Electron. Mater.*, 2023, **5**, 3685–3697.

21 J.-Y. Shao, B.-B. Cui, J.-H. Tang and Y.-W. Zhong, *Coord. Chem. Rev.*, 2019, **393**, 21–36.

22 Q. Zhang, D. Wu, Y. Fu, J. Li, Y. Chen and B. Zhang, *ACS Appl. Mater. Interfaces*, 2024, **16**, 22217–22228.

23 R. Gupta, J. A. Fereiro, A. Bayat, A. Pritam, M. Zharnikov and P. C. Mondal, *Nat. Rev. Chem.*, 2023, **7**, 106–122.

24 A. Ghoshal, R. Kaur, S. Sanju, A. K. Singh and P. C. Mondal, *J. Mater. Chem. C*, 2025, **13**, 7307–7317.

25 P. Sachan, P. Sharma, R. Kaur, D. Manna, S. Sahay and P. C. Mondal, *Small Methods*, 2025, 2401911.

26 R. Gupta, P. Jash and P. C. Mondal, *J. Mater. Chem. C*, 2021, **9**, 11497–11516.

27 S. Sinha, M. Sahad E, R. Mondal, S. Das, L. T. Manamel, P. Brandão, B. de Bruin, B. C. Das and N. D. Paul, *J. Am. Chem. Soc.*, 2022, **144**, 20442–20451.

28 R. Gupta, A. Malik, P. Sachan, A. Ghoshal, K. Kumari, S. K. Singh, L. Mena and P. C. Mondal, *Adv. Funct. Mater.*, 2024, 2415740.

29 B. Pradhan and S. Das, *Chem. Mater.*, 2008, **20**, 1209–1211.

30 S. Goswami, A. J. Matula, S. P. Rath, S. Hedström, S. Saha, M. Annamalai, D. Sengupta, A. Patra, S. Ghosh, H. Jani, S. Sarkar, M. R. Motapothula, C. A. Nijhuis, J. Martin, S. Goswami, V. S. Batista and T. Venkatesan, *Nat. Mater.*, 2017, **16**, 1216–1224.

31 M. Marcaccio, F. Paolucci, C. Paradisi, S. Roffia, C. Fontanesi, L. J. Yellowlees, S. Serroni, S. Campagna, G. Denti and V. Balzani, *J. Am. Chem. Soc.*, 1999, **121**, 10081–10091.

32 R. M. Bullock, A. K. Das and A. M. Appel, *Chem.–A Eur. J.*, 2017, **23**, 7626–7641.

33 A. Vilan, D. Aswal and D. Cahen, *Chem. Rev.*, 2017, **117**, 4248–4286.

34 C. Jia, A. Migliore, N. Xin, S. Huang, J. Wang, Q. Yang, S. Wang, H. Chen, D. Wang, B. Feng, Z. Liu, G. Zhang, D.-H. Qu, H. Tian, M. A. Ratner, H. Q. Xu, A. Nitzan and X. Guo, *Science*, 2016, **352**, 1443–1445.

35 S. Pazos, X. Xu, T. Guo, K. Zhu, H. N. Alshareef and M. Lanza, *Nat. Rev. Mater.*, 2024, **9**, 358–373.

36 V. Singh, P. C. Mondal, A. K. Singh and M. Zharnikov, *Coord. Chem. Rev.*, 2017, **330**, 144–163.

37 J. Song, A. Jancik-Prochazkova, K. Kawakami and K. Ariga, *Chem. Sci.*, 2024, **15**, 18715–18750.

38 A. J. Bergren, R. L. Mccreery, S. R. Stoyanov, S. Gusarov and A. Kovalenko, *J. Phys. Chem. C*, 2010, 15806–15815.

39 R. Gupta, A. Malik, K. Kumari, S. K. Singh, V. Vivier and P. C. Mondal, *Chem. Sci.*, 2024, **15**, 8775–8785.

40 N. Singh, A. Malik, P. Sethi and P. C. Mondal, *Small*, 2024, 03108.
41 C. R. Peiris, Y. B. Vogel, A. P. Le Brun, A. C. Aragonès, M. L. Coote, I. Díez-Pérez, S. Ciampi and N. Darwish, *J. Am. Chem. Soc.*, 2019, **141**, 14788–14797.
42 D. Frath, V. Q. Nguyen, F. Lafolet, P. Martin and J. C. Lacroix, *Chem. Commun.*, 2017, **53**, 10997–11000.
43 N. Darwish, P. K. Eggers, S. Ciampi, Y. Tong, S. Ye, M. N. Paddon-Row and J. J. Gooding, *J. Am. Chem. Soc.*, 2012, **134**, 18401–18409.
44 P. Sachan and P. C. Mondal, *Analyst*, 2020, **145**, 1563–1582.
45 R. Gupta, S. Bhandari, S. Kaya, K. P. Katin and P. C. Mondal, *Nano Lett.*, 2023, **23**, 10998–11005.
46 T. Kurita, Y. Nishimori, F. Toshimitsu, S. Muratsugu, S. Kume and H. Nishihara, *J. Am. Chem. Soc.*, 2010, **132**, 4524–4525.
47 M. Supur, S. R. S. R. Smith and R. L. R. L. McCreery, *Anal. Chem.*, 2017, **89**, 1–24.
48 S. R. Smith and R. L. McCreery, *Adv. Electron. Mater.*, 2018, **4**, 1800093.
49 P. Saha, M. Sahad E, S. Sathyanarayana and B. C. Das, *ACS Nano*, 2024, **18**, 1137–1148.
50 R. L. McCreery, *Acc. Chem. Res.*, 2022, **55**, 2766–2779.
51 I. Hnid, D. Frath, F. Lafolet, X. Sun and J.-C. Lacroix, *J. Am. Chem. Soc.*, 2020, **142**, 7732–7736.
52 T. Asset, A. G. Oshchepkov and G. A. Tsirlina, *Electrochim. Acta*, 2024, **507**, 145174.
53 S. Rahpeima, A. Le, C. L. Raston and N. Darwish, *J. Colloid Interface Sci.*, 2022, **626**, 985–994.
54 P. Sachan, P. Makkar, A. Malik and P. C. Mondal, *J. Mater. Chem. C*, 2024, **12**, 13639–13650.
55 M. J. Frisch, G. W. Trucks, H. B. Schlegel, G. E. Scuseria, M. A. Robb, J. R. Cheeseman, G. Scalmani, V. Barone, B. Mennucci, G. A. Petersson, H. Nakatsuji, M. Caricato, X. Li, H. P. Hratchian, A. F. Izmaylov, J. Bloino, G. Zheng, J. L. Sonnenberg, M. Hada, M. Ehara, K. Toyota, R. Fukuda, J. Hasegawa, M. Ishida, T. Nakajima, Y. Honda, O. Kitao, H. Nakai, T. Vreven, J. A. Montgomery Jr, F. Ogliaro, M. Bearpark, J. J. Heyd, E. Brothers, K. N. Kudin, V. N. Staroverov, R. Kobayashi, J. Normand, K. Raghavachari, A. Rendell, J. C. Burant, S. S. Iyengar, J. Tomasi, M. Cossi, N. Rega, J. M. Millam, M. Klene, J. E. Knox, J. B. Cross, V. Bakken, C. Adamo, J. Jaramillo, R. Gomperts, R. E. Stratmann, O. Yazyev, A. J. Austin, R. Cammi, C. Pomelli, J. W. Ochterski, R. L. Martin, K. Morokuma, V. G. Zakrzewski, G. A. Voth, P. Salvador, J. J. Dannenberg, S. Dapprich, A. D. Daniels, Ö. Farkas, J. B. Foresman, J. V. Ortiz, J. Cioslowski, and D. J. Fox, *Gaussian 09*, Revision B.01, Gaussian, Inc., Wallingford, CT, 2009.
56 D. Andrae, U. Huermann, M. Dolg, H. Stoll and H. Preu, *Theor. Chim. Acta*, 1990, **77**, 123–141.
57 V.-V. V. Hugo, H.-S. M. Alejandro, V.-S. A. María, R.-H. María, L.-R. M. Antonio, P.-O. M. Guadalupe, M.-G. M. Antonio, A.-H. Fernando, A. Víctor, C.-A. Diego and Á. Enrique, *Comput. Chem.*, 2019, **07**, 1–26.
58 A. Vlček and S. Záliš, *Coord. Chem. Rev.*, 2007, **251**, 258–287.
59 S. Karmakar, D. Maity, S. Mardanya and S. Baitalik, *Dalton Trans.*, 2015, **44**, 18607–18623.
60 D. N. G. Krishna and J. Philip, *Appl. Surf. Sci. Adv.*, 2022, **12**, 100332.
61 A. G. Shard, *J. Vac. Sci. Technol., A*, 2020, **38**, 041201.
62 D. S. Faber and A. E. Pereda, *Front. Mol. Neurosci.*, 2018, **11**, 1–11.
63 C. Hammond, *Cellular and Molecular Neurophysiology*, Elsevier, 4th edn, 2015.
64 E. D. Gribkova and R. Gillette, *Sci. Rep.*, 2021, **11**, 1–16.
65 A. Citri and R. C. Malenka, *Neuropsychopharmacology*, 2008, **33**, 18–41.
66 T. V. P. Bliss and G. L. Collingridge, *Mol. Brain*, 2013, **6**, 1–14.
67 R. Wells, *Soft Comput.*, 2003, 1–13.
68 L. Wang, H. Zhu and D. Wen, *Ceram. Int.*, 2021, **47**, 33865–33874.
69 M. A. Lampert, *Rep. Prog. Phys.*, 1964, **27**, 307.
70 J. A. Geurst, *Phys. Status Solidi*, 1966, **15**, 107–118.
71 Y. Sun, L. Li, D. Wen, X. Bai and G. Li, *Phys. Chem. Chem. Phys.*, 2015, **17**, 17150–17158.
72 Y. Beilliard, F. Paquette, F. Brousseau, S. Ecoffey, F. Alibart and D. Drouin, *AIP Adv.*, 2020, **10**, 025305.
73 M. Xue, S. Kabehie, A. Z. Stieg, E. Tkatchouk, D. Benitez, R. M. Stephenson, W. A. Goddard, J. I. Zink and K. L. Wang, *Appl. Phys. Lett.*, 2009, **95**, 093503.
74 S. A. Mazen and A. M. El Taher, *J. Alloys Compd.*, 2010, **498**, 19–25.
75 P. C. Mondal, U. M. Tefashe and R. L. McCreery, *J. Am. Chem. Soc.*, 2018, **140**, 7239–7247.
76 P. Jash, R. K. Parashar, C. Fontanesi and P. C. Mondal, *Adv. Funct. Mater.*, 2022, **32**, 2109956.
77 P. Alcamí and A. E. Pereda, *Nat. Rev. Neurosci.*, 2019, **20**, 253–271.
78 A. Bou and J. Bisquert, *J. Phys. Chem. B*, 2021, **125**, 9934–9949.
79 L. Chen, J. Li, Y. Chen, Q. Deng, J. Shen, X. Liang and L. Jiang, *Proceedings of the 2017 Design, Automation and Test in Europe*, 2017, pp. 19–24.
80 E. Zamanidoost, F. M. Bayat, D. Strukov and I. Kataeva, *IEEE International Symposium on Intelligent Signal Processing (WISP)*, 2015, pp. 1–6.
81 Z. Cao, B. Sun, G. Zhou, S. Mao, S. Zhu, J. Zhang, C. Ke, Y. Zhao and J. Shao, *Nanoscale Horiz.*, 2023, **8**, 716–745.
82 J. John, K. Ramesh and P. Velayudhaperumal Chellam, in *Advanced Materials for Sustainable Environmental Remediation*, Elsevier, 2022, pp. 155–174.
83 P. Cassoux, L. Valade and P.-L. Fabre, in *Comprehensive Coordination Chemistry II*, Elsevier, 2003, pp. 761–773.